

# Surface Roughness Gradients Reveal Topography-Specific Mechanosensitive Responses in Human Mesenchymal Stem Cells

Yong Hou, Wenyan Xie, Leixiao Yu,\* Luis Cuellar Camacho, Chuanxiong Nie, Man Zhang, Rainer Haag, and Qiang Wei\*

The topographic features of an implant, which mechanically regulate cell behaviors and functions, are critical for the clinical success in tissue regeneration. How cells sense and respond to the topographical cues, e.g., interfacial roughness, is yet to be fully understood and even debatable. Here, the mechanotransduction and fate determination of human mesenchymal stem cells (MSCs) on surface roughness gradients are systematically studied. The broad range of topographical scales and high-throughput imaging is achieved based on a catecholic polyglycerol coating fabricated by a one-step-tilted dip-coating approach. It is revealed that the adhesion of MSCs is biphasically regulated by interfacial roughness. The cell mechanotransduction is investigated from focal adhesion to transcriptional activity, which explains that cellular response to interfacial roughness undergoes a direct force-dependent mechanism. Moreover, the optimized roughness for promoting cell fate specification is explored.

converts physical cues in microniche to intracellular biochemical signals that are recognized by cells.<sup>[3]</sup> In general, these physical stimuli promote integrin activation and focal adhesion (FA) formation as well as the alignment of cytoskeletal and nucleoskeletal elements, providing structural support and function. In parallel, the signaling cascades are initiated under cellular contraction to activate transcription factors. The cellular force and signaling proteins further regulate gene expression synergistically to control cellular functions and phenotypes.<sup>[4,5]</sup>

The topography of ECM has been shown to act as one of the important physical cues to dictate cell adhesion and differentiation.<sup>[6]</sup> Understanding cell

## 1. Introduction

Extracellular matrix (ECM), a network of fibrillar proteins and polysaccharides, anchors cells and directs cell functions through not only biochemical signals but also mechanical and topographic cues.<sup>[1,2]</sup> These physical cues mediate cell behaviors via mechanotransduction, a process that integrates and

responses to their natural environment can guide the design of biomimetic materials for modulating cell behaviors in regenerative therapeutics. Over the past two decades, a wide range of substrates with surface roughness from nano- to microscale has been developed to investigate the effects of topography. However, most of these studies were performed based on a few model surfaces with discontinuous different roughness. Many of the conclusions are suitable for the specific conditions as presented but are likely to be inconsistent with each other for becoming a general conclusion. For instance, the titanium surface with small roughness like 15 nm in height rather than 55 and 100 nm was noticed to promote the adhesion and osteogenesis of mesenchymal stem cells (MSCs) in one report.<sup>[7]</sup> However, the optimized roughness to do so was 150 and 450 nm rather than 20 nm on the same type of materials in another report.<sup>[8]</sup> Moreover, no difference was observed for the adhesion of osteoblasts on the titanium surfaces with different roughness in one other case.<sup>[9]</sup> Such discrepancies may attribute to the lacking of a high-throughput strategy to examine the effects with a broad range of roughness, because the fabrication of a rough surface is normally complicated and time-consuming.

As an alternative, surfaces with roughness gradients can be highlighted in the study of cell mechanoresponsive and may allow us to optimize the topographic features for cell functions. In fact, a few gradient surfaces have been generated to screen cell response to interfacial roughness.<sup>[10,11]</sup> However, the cellular mechanotransduction has not been investigated in depth. Therefore, the underlying mechanism of how topography signals modulate cell behaviors has not been fully understood.

Y. Hou, Dr. L. Yu, Dr. L. C. Camacho, C. Nie, Prof. R. Haag  
 Institute of Chemistry and Biochemistry  
 Freie Universität Berlin  
 Takustr. 3, 14195 Berlin, Germany  
 E-mail: leixiaoyu@zedat.fu-berlin.de

Dr. W. Xie  
 Institute of Pharmacy  
 Freie Universität Berlin  
 Königin-Luise-Str. 2 + 4, 14195 Berlin, Germany

M. Zhang, Prof. Q. Wei  
 College of Polymer Science and Engineering  
 State Key Laboratory of Polymer Materials and Engineering  
 Sichuan University  
 610065 Chengdu, China  
 E-mail: wei@scu.edu.cn

 The ORCID identification number(s) for the author(s) of this article can be found under <https://doi.org/10.1002/smll.201905422>.

© 2020 The Authors. Published by WILEY-VCH Verlag GmbH & Co. KGaA, Weinheim. This is an open access article under the terms of the Creative Commons Attribution License, which permits use, distribution and reproduction in any medium, provided the original work is properly cited.

DOI: 10.1002/smll.201905422

In this study, roughness gradient surfaces covering a wide range of roughness from nanometer to micrometer were produced by a one-step-tilted dip-coating approach with a catecholic polymer. The impact of roughness on cell morphology, mechanotransduction, and fate determination was systematically investigated. The activation of FA structural proteins and signaling proteins, the organization of cytoskeleton, the cell nuclear mechanics, as well as the transcriptional activity were analyzed in depth to reveal the mechanism of MSC response to interfacial topographic features. Our results will guide the design of interfacial mechanical cues that regulate cell functions in stem cell engineering and regenerative medicine.

## 2. Results and Discussion

### 2.1. Surface with Roughness Gradient

Catecholic polyglycerol, which mimics mussel foot proteins, was recognized as the second generation of mussel-inspired adhesive to fabricate universal coatings with versatile functions.<sup>[12]</sup> It can rapidly adhere on virtually all kinds of material surfaces with tunable coating thickness and morphology benefiting

from its heteromultivalent character, distinct “interior,” and appropriate molecular weight. The efficient cross-linking and aggregation of the polymers result in the fast deposition of the aggregated nanoparticles onto substrates. The number of the stacked particles on each other and their density, i.e., the growth of the aggregates, can be controlled by the adjustment of the depth during the coating. Thus, the aggregates on the deeper location of the glass slides grew larger, which caused higher roughness.<sup>[13]</sup> Consequently, a coating with gradient roughness was achieved by simply tilting the glass substrate in the polymer solution (Figure 1A). In addition, benefiting from the large number of amine and catechol groups on the coating surfaces, the coatings could support cell adhesion without treatment with ECM proteins.<sup>[12]</sup>

The morphology of the roughness gradient surface was characterized by scanning electron microscopy (SEM) and atomic force microscopy (AFM). Both techniques indicated the gradient progression from flat (position RG<sub>5%</sub>) to rough (position RG<sub>95%</sub>) topography on the surface (Figure 1B,C and Figure S1A, Supporting Information). Specifically, the roughness gradients showed nanometer amplitude features from the position RG<sub>5%</sub> to RG<sub>50%</sub> with average roughness ( $R_a$ ) 53.86 to 278.64 nm and root mean square roughness ( $R_q$ ) 31.49 to

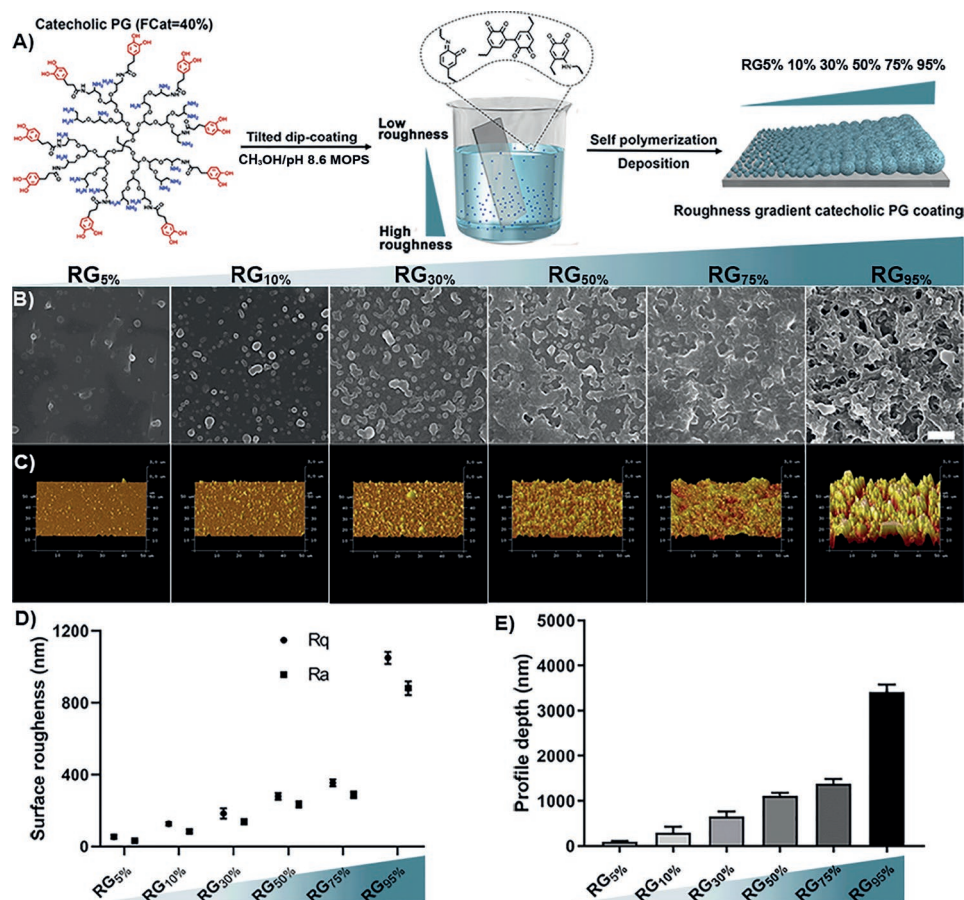


**Figure 1.** Fabrication and characterization of the surfaces with roughness gradient. A) Scheme of the fabrication of roughness gradient via one-step tilted dip-coating approach. B) SEM and C) AFM 3D images of the surface morphology of roughness gradient at different positions. Scale bar corresponds to 5  $\mu\text{m}$  for SEM images and 10  $\mu\text{m}$  for AFM images. D)  $R_a$  and  $R_q$  values of roughness gradient at different positions according to AFM images. E) Quantification of the average depth of profile elements within the gradient roughness surfaces.

234.41 nm in a linear trend. From  $RG_{75\%}$  to  $RG_{95\%}$ , the roughness rapidly increased in the submicrometer range from 353.66 to 1050.31 nm for  $R_a$  and from 287.55 to 881 nm for  $R_q$ .

The roughness gradient ratio ( $R_a$ ) is about 0.01–0.05 nm  $\mu\text{m}^{-1}$  from  $RG_{5\%}$  to  $RG_{75\%}$ , and 0.11 nm  $\mu\text{m}^{-1}$  from  $RG_{75\%}$  to  $RG_{95\%}$  (Figure S2, Supporting Information). Thus, the difference of surface roughness in the length scale of a single spread cell (50–100  $\mu\text{m}$ ) was approximately 2.04 nm in the regime with low and intermediate roughness ( $RG_{5\%}$  to  $RG_{75\%}$ ) and 7.12 nm in the regime with high roughness ( $RG_{75\%}$  to  $RG_{95\%}$ ), which were smaller than the size of a single integrin (8–12 nm) that can be ignored (Figure 1D).<sup>[14]</sup> Therefore, cells should not sense the polarized signal inputs on this roughness gradient surface. The mean depth of the profile elements gradually varied from 99 nm to 3.42  $\mu\text{m}$ , corresponding to the controlled stacked structure toward the increasing roughness of the gradient (Figure 1E and Figure S1B, Supporting Information).

The thickness of the polymer coating in the region of  $RG_{5\%}$  was about 50 nm (Figure S1B, Supporting Information). Owing to the high density and rigidity of the aggregates of catecholic polyglycerol,<sup>[12]</sup> the chemical and mechanical properties of the underneath glass support layer can be shielded by gradient coatings. Thus, cells can only sense homogenous rigidity and chemical cues. Moreover, mussel-inspired surfaces exhibit good biocompatibility and promote cell adhesion.<sup>[15]</sup> Thus, we have generated a model surface with gradient topographic features to study cell behaviors.

## 2.2. Interfacial Roughness Mediates Cell Adhesion

To investigate the cell adhesion on rough surface, MSCs were seeded and cultured for 24 h. As shown in Figure 2A–C, the cell spreading area gradually decreased (from 3355 to 614  $\mu\text{m}^2$ ) and cell circularity gradually increased (from 0.385 to 0.625), when the substrate roughness increased from  $RG_{5\%}$  to  $RG_{95\%}$ . The pronounced actin stress fibers were observed in the relatively low roughness region between  $RG_{5\%}$  and  $RG_{50\%}$ , while smaller and decreased bundles were displayed in the relatively high roughness region between  $RG_{75\%}$  and  $RG_{95\%}$  (Figure 2F).

More details of cell morphology were exhibited in SEM images (Figure 2E). The length and density of filopodia were varied according to roughness increase (Figure 2D). Cells expressed a few but clear filopodia with average length of 4.24  $\mu\text{m}$  in the region  $RG_{5\%}$  with lowest roughness. Meanwhile, filopodia formation was largely limited in the region  $RG_{95\%}$  with highest roughness. The longest as well as densest filopodia were observed in the region  $RG_{50\%}$  with intermediate roughness. The average length reached 9.29  $\mu\text{m}$ , which was 1.96-fold and 2.93-fold longer than that on  $RG_{5\%}$  and  $RG_{95\%}$ , respectively. Filopodia, which are highly organized and tightly cross-linked long bundles of actin filaments,<sup>[16]</sup> enable cells to sense the nano/micro topographic features and guide cell adhesion via filopodia traction forces.<sup>[16,17]</sup>

The 3D-reconstructive morphology of the basal surface of cells was obtained by confocal laser scanning microscopy with the multiple z-stack imaging mode. It is obvious that the basal surface of cells was remodeled by the substrate and cell surface roughness was increased with substrate roughness

(Figure 2G). Especially, the actin networks invaded the large cave structure of the surface in the highly rough region ( $RG_{75\%}$  to  $RG_{95\%}$ ), which may limit cell extension in horizontal direction.<sup>[18]</sup> These results agree with some previous reports that the geometry factor of the discontinuities acted as an energy barrier. The cells try to adapt themselves with the defined surface morphologies to minimize the contact with the high energy discontinuities.<sup>[19,20]</sup> This hindered cell FA formation, actin polymerization, and thus limited filopodia formation and cell spreading. Whereas cells adhered on the surface with relatively low roughness ( $RG_{5\%}$ – $RG_{50\%}$ ) can overcome the topographical features during spreading, as the size of the aggregated particles on coating surface was far smaller than cell dimension.

Cell adhesion may also be ascribed to the spatial properties of the aggregated nanoparticle on the roughness gradient surface. In general, the diameter of integrin is about 8–12 nm and the integrin clustering is larger than 1  $\mu\text{m}$ .<sup>[14,21]</sup> The nanoscale particles corresponded to the sizes of proteins and cell membrane receptors. The microscale aggregates corresponded to the sizes of receptor clusters. The optimized hierarchical structures combining both micro- and nanoscale roughness displayed increased surface area that benefited protein adsorption to enhance the cell-to-substrate affinity.<sup>[22]</sup>

## 2.3. Cells Sense Interfacial Roughness through FA and Actomyosin Cytoskeleton

The mechanical properties of ECM can be sensed by the force-sensing molecules in FAs, which convert the physical signals into intracellular biochemical signals to induce cellular contractility through cytoskeletons.<sup>[23,24]</sup> The cells contract their actomyosin cytoskeleton generating mechanical forces at the sites of adhesion in order to maintain their cytoskeleton in a state of mechanical tension or prestress.<sup>[19]</sup> The nanoscale structures on the bio-surfaces show great effect on the formation of FAs. For example, anisotropic nanoscale presentation of cell adhesion ligand enhances the recruitment of diverse integrins in adhesion structures and enables the mature FAs toward fibrillar adhesion.<sup>[25]</sup> The expression and arrangement of FAs mirror the cellular contractility and could directly reflect the level of cellular tension. We next investigated the effects of topographic roughness on FA assembly of MSCs by immunostaining of paxillin. As shown in Figure 3A,C,D the paxillin area and length gradually increased in the low roughness region and peaked at  $RG_{50\%}$ , then rapidly dropped in the high roughness region. The results are consistent with the filopodia formation, suggesting that the best cell adhesion occurs at intermediate roughness ( $RG_{50\%}$ ).

The extracellular mechanical cues can be transduced through FAs to activate signaling proteins to further regulate downstream signaling pathways, known as mechanotransduction. FA kinase (FAK), one of the key mediators in mechanotransduction pathways, can sense and respond to mechanical stimulation and regulate cell adhesion.<sup>[26]</sup> The phosphorylation of FAK is mediated by force generation and is the initial step to activate Rho family of GTPases.<sup>[27]</sup> We thus investigated the level of phosphorylated FAK (pFAK), which reflects the

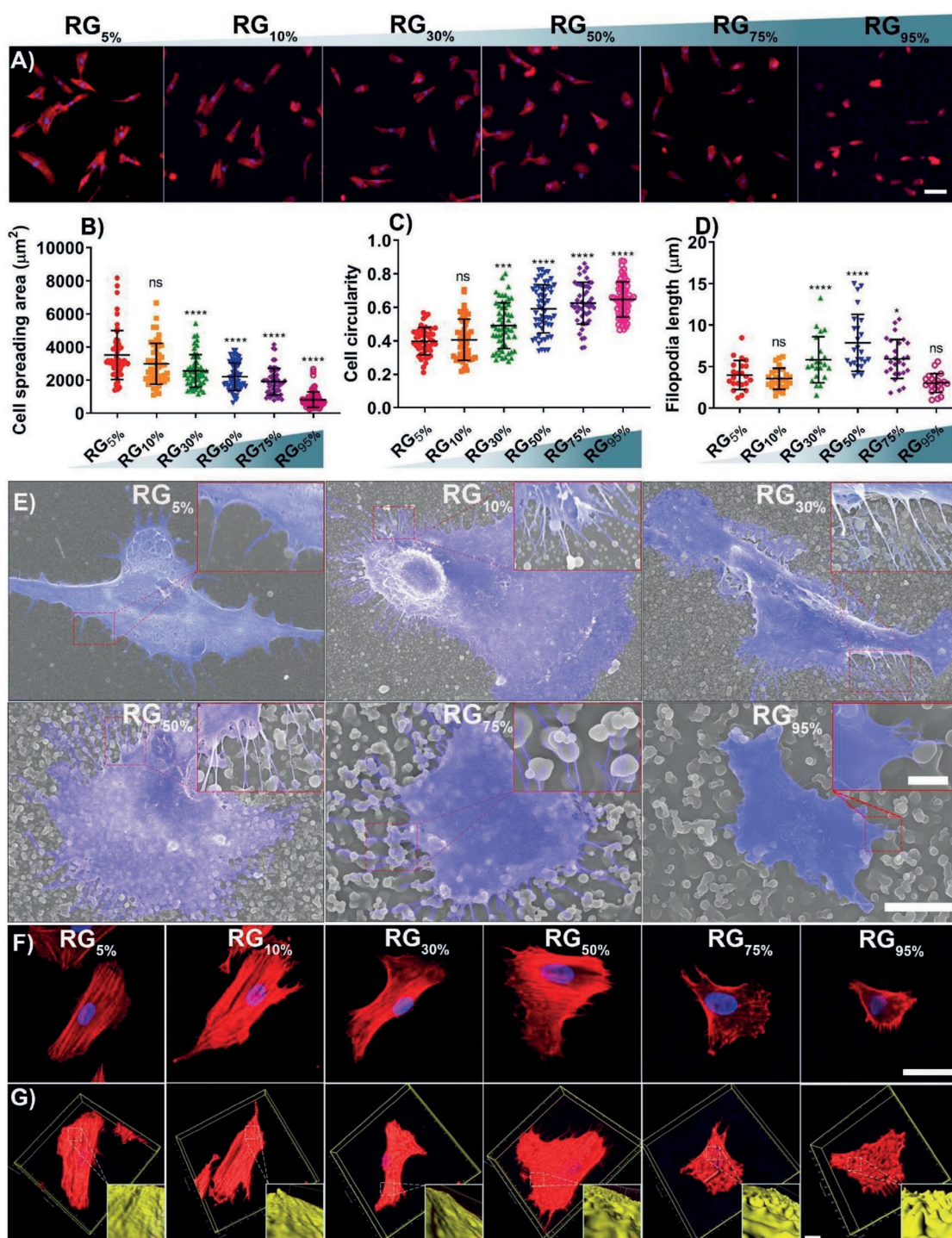


**Figure 2.** Cell adhesion on the surfaces with roughness gradient. A) Representative images of actin filaments of the MSCs cultured on roughness gradient surface for 24 h. B) Cell spreading area. C) Circularity and D) filopodia length of the adhered MSCs. E) Representative SEM images of adhered cells on roughness gradient surface (scale bar indicates 15  $\mu\text{m}$ , inset bar indicates 5  $\mu\text{m}$ ). F) Representative images of the upper-side of the cells stained with actin filaments (scale bar indicates 50  $\mu\text{m}$ ). G) 3D-reconstructed enlarged image of the basal surface of cells stained with actin filaments (scale bar indicates 25  $\mu\text{m}$ ). Insets indicated the enlarged image of the basal surface of cells.

cellular contractility generated on rough surface. As shown in Figure 3B,E the activation of pFAK was optimized at intermediate roughness ( $\text{RG}_{50\%}$ ), which was 1.39- and 1.63-folds higher than the level on  $\text{RG}_{5\%}$  and  $\text{RG}_{95\%}$ , respectively. The pFAK level

confirmed that the cells exhibited largest cellular contractility at intermediate roughness ( $\text{RG}_{50\%}$ ). In addition, it has been reported that pFAK activates Cdc42, a Rho family GTPase, leading to filopodia formation.<sup>[27–29]</sup>

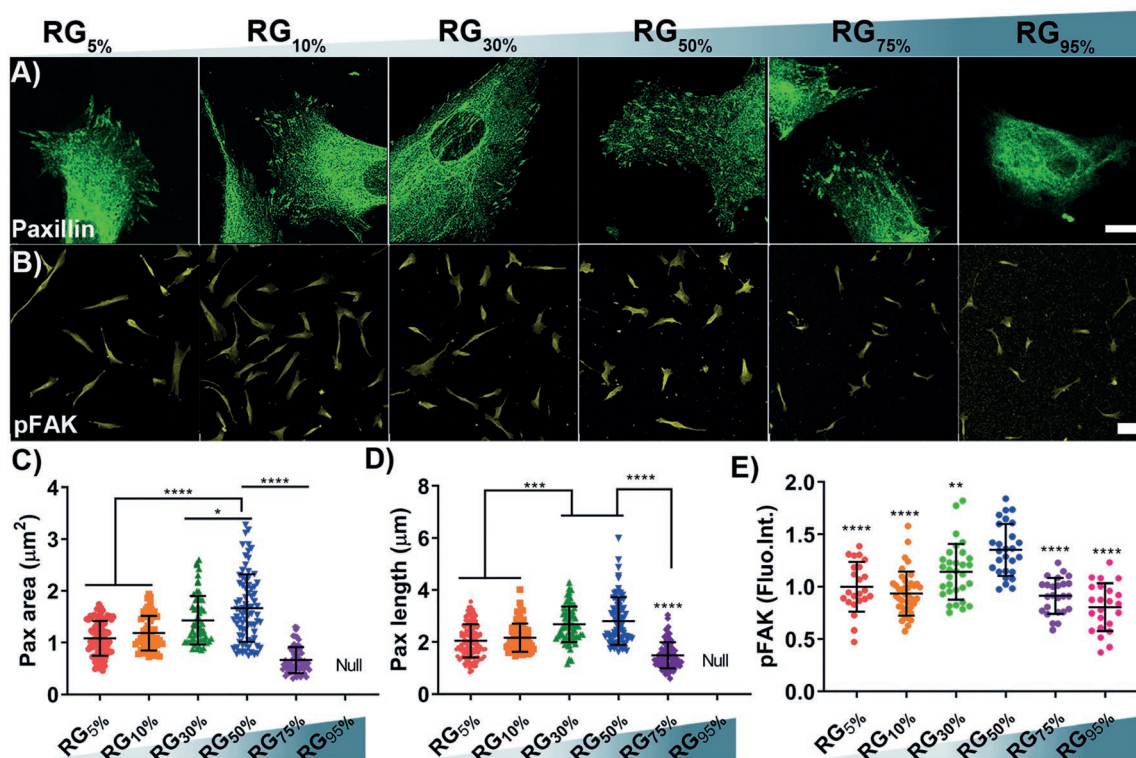


**Figure 3.** Cells sense interfacial roughness through FAs. A) Representative fluorescence images of Paxillin immunostaining for MSCs (scale bar indicates 10 µm). B) Representative fluorescence images of pFAK immunostaining for MSCs (scale bar indicates 50 µm). C, D) The area and length of the FA points of MSCs as indicated by paxillin immunostaining. E) Relative average fluorescent intensity of pFAK in MSCs. MSCs were cultured on roughness gradient surface for 24 h before paxillin or pFAK immunostaining. Mean values and standard deviations from 30 to 40 values are presented.

To confirm the role of actomyosin-based contractility in roughness sensing, myosin II inhibitor blebbistatin and actin polymerization inhibitor cytochalasin D were utilized to treat the cells on roughness gradient surfaces. The difference of cell spread area on the whole range of the gradients displayed an obvious reduction after 24 h of treatment, indicating the importance of actomyosin contractility in topography-induced cell adhesion and spreading (Figure S3, Supporting Information).

The results together suggested that the roughness-induced MSC adhesion underwent a force-dependent mechanism through the phosphorylation of FAK. We next wanted to study the transduction of topographical signals to cell nucleus, which directly mediated cell phenotypic diversity.

#### 2.4. Cell Nuclear Mechanics Responds to Topographical Roughness

As an important part in mechanotransduction and where transcription takes place, the cell nucleus, besides the cytoskeleton, is another main contributor to the cellular mechanical properties and bioactivities.<sup>[30,31]</sup> The mechanical signals are transmitted from sites of matrix adhesion to nucleus through actin cap and linker of nucleoskeleton and cytoskeleton complex.<sup>[32]</sup> The nucleoskeleton can be further activated under force and regulates the conformation of DNA or chromatin structures as well as the transcriptional activities.<sup>[33,34]</sup> Lamin A/C are intermediate filament proteins found in nearly all cell

nuclei to determine nuclear shape and size. Lamin A/C resist nuclear deformation and contribute to nuclear mechanics and stability.<sup>[32,35]</sup> Therefore, the lamin A/C could be considered as sensors for nuclear mechanics.<sup>[33]</sup> Therefore, we monitored the response of actin cap and the nucleoskeletal components lamin A/C to interfacial roughness.

The cells adhered in the low roughness region from RG<sub>5%</sub> to RG<sub>50%</sub> exhibited dense and aligned actin cap fibers. In contrast, the actin cap formation was suppressed in the high roughness region from RG<sub>75%</sub> to RG<sub>95%</sub> due to the lack of cellular contractility (Figure 4A). The confocal images of lamin A/C in cell nucleus are shown in Figure 4B,C. The nuclei were large and smooth in the region from RG<sub>5%</sub> to RG<sub>50%</sub> with low and intermediate roughness. Highly rough nuclear surfaces with small nuclear size were observed in the rough region from RG<sub>75%</sub> to RG<sub>95%</sub>. In addition, the cells on RG<sub>50%</sub> showed the highest average fluorescent intensity of lamin A/C. As reported previously, the nuclear envelope appeared highly wrinkled with low lamin A/C expression, when cells adhered on soft matrix with lower cellular tension. Meanwhile, cells adhered on stiff matrix exhibited aligned stress fibers with high tension would “smoothed out” nuclear wrinkles and flatten the nucleus with enriched lamin A/C.<sup>[32,36]</sup> A recent report showed that lamin A/C also mediated the actin cap formation to protect the nucleus from the extracellular mechanical stress. Low lamin A/C level resulted in the nuclear deformation.<sup>[37]</sup>

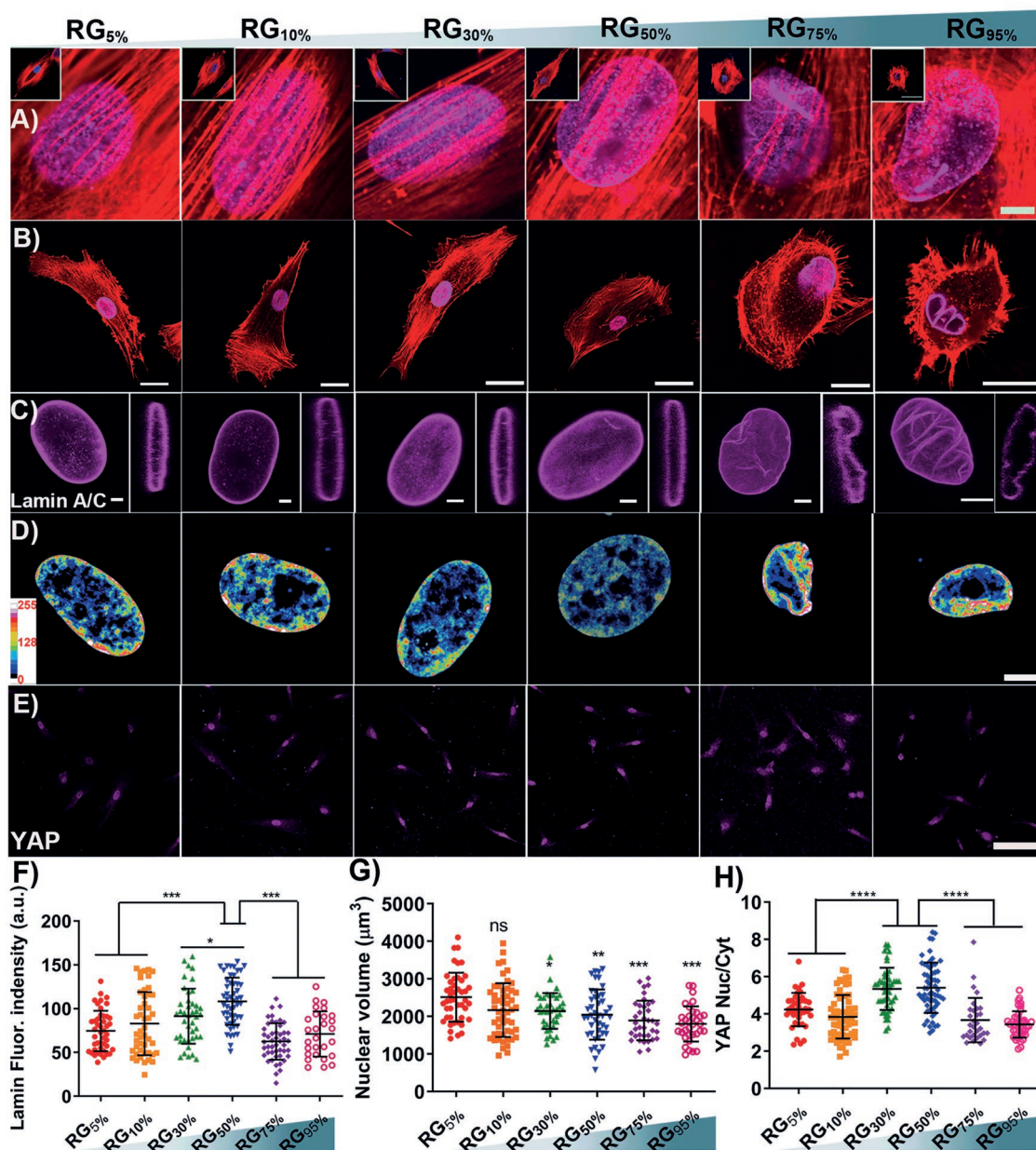


**Figure 4.** Interfacial roughness regulates cell nuclear mechanics and transcriptional activity. A) Organization of actin filaments in the apical region of the nucleus. Insets display the actin organization of MSCs (scale bar indicates 5  $\mu\text{m}$ ). B,C) Representative confocal images of cell and nuclear morphology as indicated by lamin A/C (B scale bar indicates 25  $\mu\text{m}$ , C scale bar indicates 2  $\mu\text{m}$ ). D) Chromatin condensation visualized by creating a heatmap of the DAPI intensity clusters within the nucleus (scale bar indicates 2  $\mu\text{m}$ ). E) Representative fluorescence images of YAP immunostaining for MSCs (scale bar indicates 100  $\mu\text{m}$ ). F) Quantification of lamin A/C level of MSCs on the roughness gradient surfaces by immunofluorescence at 24 h. G) Nuclear volume. H) Ratiometric analysis of nuclear localization of YAP by nuclear/cytoplasmic fluorescence intensity ratio. Mean values and standard deviations from 30 to 40 values are presented.

Furthermore, blebbistatin and cytochalasin D were used to interrupt the myosin activity and actin network organization. With inhibitor treatment, the cells on the whole range of the gradients exhibited dramatic decrease of lamin A/C expression and wrinkled morphology of nucleus (Figure S4, Supporting Information), indicating the cellular contractility was transmitted into nucleus to regulate nuclear mechanics through lamin A/C.

## 2.5. Interfacial Roughness Regulates Chromatin Remodeling and Transcriptional Regulators

Nuclear mechanics mediated by topographical features is related to the chromatin remodeling, which affects a series of fundamental cellular processes including mRNA transcription, DNA replication, recombination, repair, etc.<sup>[38]</sup> Chromatin condensation was visualized by creating heatmaps of DAPI

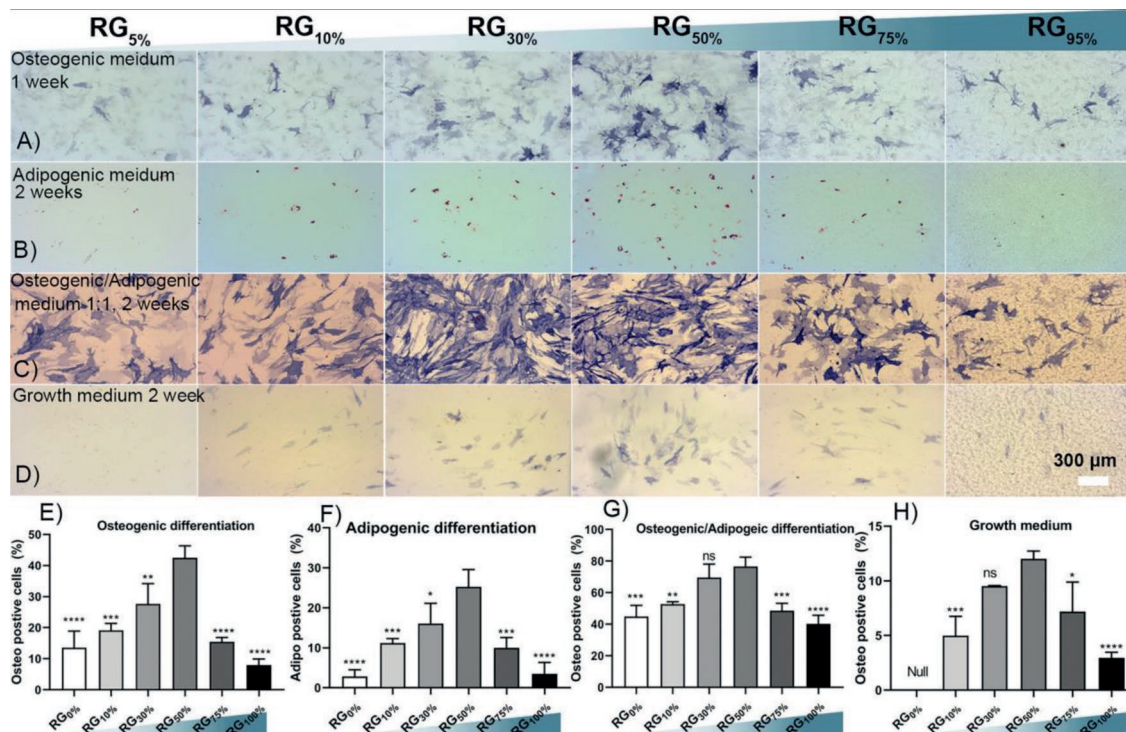


**Figure 5.** MSC (Merck, SCC034, Lot: 2590004) differentiation on roughness gradient surfaces under different culture conditions. A–D) Representative images of cells cultured in A) osteogenic (1 week, ALP staining), B) adipogenic (2 weeks, lipid staining), C) osteogenic/adipogenic 1:1 mixed (2 weeks, ALP and lipid staining), and D) growth medium (2 weeks, ALP and lipid staining). E–H) Quantitative analysis of osteogenic and adipogenic differentiation of the cells in different culture conditions. Mean values and standard deviations from three independent experiments are presented.

(4',6-diamidino-2-phenylindole) intensity to investigate the response of chromatin remodeling process to interfacial roughness features. As shown in Figure 4D, cells in a highly rough region (RG<sub>75%</sub> to RG<sub>95%</sub>) exhibited higher overall DAPI intensity and higher gene clustering level in the nucleus compared with those in smoother regions (RG<sub>5%</sub> to RG<sub>50%</sub>). The level of chromatin condensation, RG<sub>50%</sub> < RG<sub>30%</sub> ≈ RG<sub>10%</sub> ≈ RG<sub>5%</sub> < RG<sub>75%</sub> ≈ RG<sub>95%</sub>, was almost consistent with the cellular and nuclear tension as discussed above, RG<sub>50%</sub> > RG<sub>30%</sub> > RG<sub>10%</sub> ≈ RG<sub>5%</sub> > RG<sub>75%</sub> > RG<sub>95%</sub>. This indicated that chromatin remodeling in MSCs is regulated by cell mechanics that triggered by interfacial roughness features.

The transcriptional activity is known to be regulated by mechanical cues through transcriptional regulators YAP (Yes-associated protein) and TAZ (transcriptional coactivator with PDZ-binding motif, also known as WWTR1).<sup>[39]</sup> As expected, the level of YAP nuclear accumulation steadily increased with the roughness increasing till the intermediate roughness region at RG<sub>50%</sub> with maximum value 5.37, and then slowly decreased to 3.48 at RG<sub>95%</sub> (Figure 4E,H). As a result, the cell phenotype, which is mediated by chromatin remodeling and transcriptional activity, may be influenced by interfacial roughness.

## 2.6. MSC Fate Determination Is Mediated by Interfacial Roughness

The differentiation of MSCs toward osteogenesis and adipogenesis in different biochemical conditions was examined on the

roughness gradient surface (Figure 5). Interestingly, both osteogenic and adipogenic differentiation peaked at intermediate roughness region RG<sub>50%</sub> in the related single induction media (Figure 5A,B,E,F). However, adipogenic differentiation was suppressed and osteogenic differentiation was promoted by interfacial roughness in either 1:1 mixed osteogenic/adipogenic media (Figure 5C,G) or growth media (Figure 5D,H). It must be noted that the adipogenic differentiation was not detected in these media. Thus, certain roughness could enhance the osteogenic differentiation of MSCs. The optimized roughness was in the intermediate region RG<sub>50%</sub>, where the highest cellular and nuclear tension of the adhered MSCs was noticed.

Normally, the cells displaying high YAP nuclear localization prefer osteogenesis and the adipogenesis is compressed.<sup>[40]</sup> However, the adipogenesis signaling pathway is totally different from osteogenesis. The YAP nuclear localization is not the only conclusive factor to regulate the MSC adipogenic differentiation. The enhancement of osteogenesis and adipogenesis in the same condition was reported in a few previous reports. Wagner et al. found the nanopatterns with a periodicity of 650 nm increased differentiation toward both osteogenic and adipogenic lineages.<sup>[41]</sup> In another study, Cameron et al. indicated MSCs cultured on the substrates with loss modulus of 130 Pa showed significant increase in the expression of both adipogenic and osteogenic markers compared with on the substrates with loss modulus of 1 Pa.<sup>[42]</sup> It might speculate that the complex surface topography and chemistry triggered different signaling pathways to promote osteogenic and adipogenic differentiation,

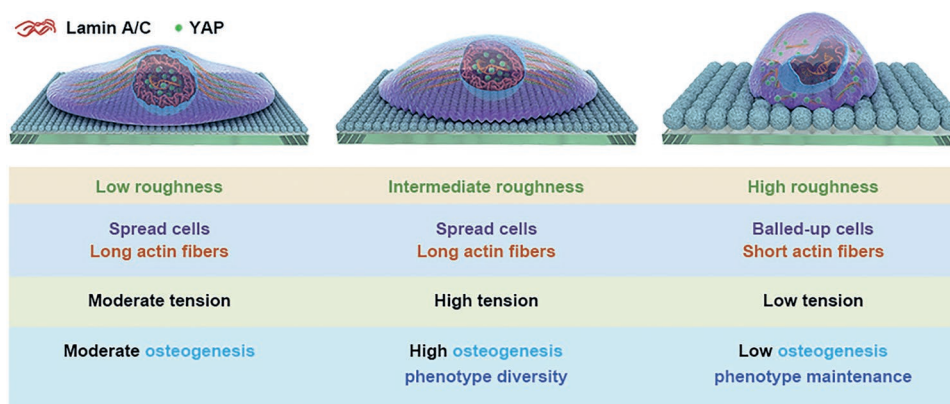


**Figure 6.** Cell fate determination regulated by surface roughness. MSCs cultured on the surface with intermediate roughness exhibit extensive cell spreading and high cellular tension to enhance the osteogenic differentiation and cellular phenotype diversity. The adhesion of MSCs on the surface with high roughness is limited, but the cells can maintain their phenotype.

respectively. The underlying molecular mechanism still remains challenging and will be further investigated in the future.

Interestingly, both osteogenic and adipogenic differentiation were limited in the region RG<sub>95%</sub> with the highest roughness. Certain reduction in adhesion can prevent metabolome activation with associated energy demand required for differentiation.<sup>[43]</sup> The high roughness region in our system may limit cell adhesion to the right range to maintain the phenotype of MSCs. A micro–nano hierarchical roughness of the surface was identified to promote the maintenance of undifferentiated embryonic stem cells.<sup>[44]</sup> In order to strengthen the conclusion, different source (Figure S5, Supporting Information) and different passage number (Figure S6, Supporting Information) of MSCs were employed to repeat the osteogenic and adipogenic differentiation experiments. The same trend and similar performance were observed. Thus, the experimental results were not caused by the variability of the cell differentiation ability.

Overall, the adhesion and fate specification of MSCs respond to interfacial roughness through mechanotransduction pathways including FA formation, activation of signaling proteins, nuclear tension generation, chromatin remodeling, and transcriptional activity (Figure 6).

### 3. Conclusion

In summary, roughness gradient surfaces with a broad variety of topographic roughness from nano- to microscale were fabricated with a mussel-inspired polymer and a one-step-tilted dip-coating approach. This easy-to-use material platform exhibits homogenous surface chemistry and mechanical rigidity with topographic diversity, which provides the broad range of topographical scales and high-throughput for imaging. It allows us to understand how cells sense and respond to interfacial topography. The results extend the knowledge that the cooperation between cell extension in a horizontal and invasion in vertical direction mediates cell adhesion on the surfaces with such complex micro/nano structures. Although the cell spreading area exhibited a linear correlation with the interfacial roughness, the formation of FAs and filopodia as well as cellular tension generation showed a biphasic manner and was optimized

in the region with intermediate roughness. As expected, the osteogenic differentiation was also enhanced in the same region as the result of high nuclear tension and transcriptional activity. Benefiting from such a high-throughput platform, a highly rough region was identified to maintain the phenotype of MSCs by reducing cell adhesion to certain level. In general, the topographic cues are sensed by cell adhesion proteins and transduced through force-sensing signaling proteins, e.g., FAK, and actin stress fibers including actin cap to regulate nuclear tension. The cell fate determination is directly mediated by the chromatin remodeling and transcriptional activity, which are initiated by cellular force generation. Our study highlights a tool for topographically gradient surfaces and defines cellular behavior on material surfaces with certain topographic features. It may provide new insight into the design of biomaterials and assist the development of biomedical engineering.

### 4. Experimental Section

*Preparation of Catecholic Polyglycerol Coating with Roughness Gradient:* The catecholic polyglycerol was obtained from the amide coupling reaction between 3,4-dihydroxyhydrocinnamic acid and amine-functionalized hyperbranched glycerol in an acidic buffer to precisely control the grafting density and prevent the oxidation of catechol during reaction. The roughness gradient coatings were prepared by immersing the freshly cleaned glass slides in a mixture of MeOH and 3-(*N*-morpholino)-propanesulfonic acid (MOPS, 0.1 M, pH 8.6) buffer (v/v 4:1) with 0.5 mg mL<sup>-1</sup> catecholic polyglycerol overnight. The depth of the solution was 2 cm. The slides were tilted in the coating solution as shown in Figure 1. The coated slides were thoroughly rinsed with water and methanol, followed by drying with argon stream.

*Surface Characterization:* For surface morphology imaging, the dried surfaces were sputter-coated with gold and observed by SEM (Hitachi SU8030, Japan). Roughness was quantified by AFM (Nanoscope MultiMode 8) with contact model. All measurements were performed in ambient condition. Contact mode was performed for larger areas (50 μm). AFM tips SNL-10 (Bruker) with a nominal tip radius of 2–12 nm were used. Scan rates of 0.5–0.15 Hz were used during mapping with 512 points per scan.

*Cell Culture:* MSCs were purchased from EMD Millipore (Darmstadt, Germany) and cultured in Dulbecco's modified Eagle medium (Gibco 11965092) supplemented with 10% bovine growth serum (Gibco 16030074) and 1% penicillin/streptomycin (Gibco 15140122) at 37 °C with 5% CO<sub>2</sub>. The osteogenic differentiation medium (C-28013) and

adipogenic differentiation medium (C-28016) were obtained from Promo Cell (Heidelberg, Germany). The cells were passaged twice a week according to the standard protocols. The fourth to sixth passages of MSCs were used in this study.

**Immunofluorescence:** After allowing the cells to grow on the gradient surfaces for specific time, the cells were fixed with 4% formaldehyde for 30 min at room temperature, permeabilized with 0.25% Triton X-100 in phosphate buffered saline (PBS) for 10 min, and then blocked with 1% bovine serum albumin in PBST (PBS with 0.1% Triton X-100) for 45 min at room temperature. Next, the cells were incubated with primary antibodies overnight at 4 °C. The following primary antibodies were used: mouse monoclonal anti-Paxillin (BD Transduction Laboratories 612405, 1:100 dilution), rabbit monoclonal anti-YAP (Cell signaling 49125, 1:200 dilution), rabbit monoclonal anti-Phospho-FAK (Tyr397) (Thermo 700255, 1:300 dilution), mouse monoclonal anti-Lamin A/C (Thermo MA3-1000, 1:100 dilution). Cells were washed with PBS two times and then incubated with the appropriate secondary antibodies (Invitrogen, Goat anti-Mouse IgG Alexa Fluor 488 A-11029 or Goat anti-Rabbit Alexa Fluor 568 A-11011, 1:500 dilution) for 1 h at room temperature. Finally, the cells were stained with DAPI (Sigma D9542, 1:1000 dilution) and Phalloidin-iFluor 647 (Abcam ab176759, 1:1000 dilution) and imaged by Zeiss Axio Observer Z1 phalloid microscope (Zeiss, Germany) or a confocal microscope (SP8, Leica).

**3D Imaging with Confocal Microscopy:** 3D fluorescence imaging was performed using a Leica SP8 microscope to obtain 3D reconstructive images of the cell morphology (actin staining with phalloidin) and nucleus morphology (lamin A/C staining). A 63 × oil immersion objective was used. Each sample was imaged using multiple z-stack images with each step of 0.1 μm.

The nuclear volume measurement was performed using Imaris software as previously described.<sup>[45]</sup> Briefly, z-stack of confocal images of fluorescent lamin A/C was 3D-reconstructed to localize the outer surface of the nuclear envelope, where the outer surface was defined to be independent of the threshold value. 3D domain of pixels within the outer surfaces of the nucleus was integrated to obtain the value of nuclear volume.

**MSC Differentiation:** The MSCs were seeded on roughness gradient surfaces in basal growth medium with density of 5000 cell cm<sup>-2</sup> for 24 h. Afterward the medium was replaced by standard osteogenic or adipogenic differentiation medium for 7–14 days. The culture medium was replaced every 3 days. Alkaline phosphatase (ALP) and lipids were recognized as the biomarkers of osteogenesis and adipogenesis, respectively. To examine osteogenesis, cells were fixed in 4% paraformaldehyde for 5 min and then stained by Fast Blue RR/naphthol (Sigma) for ALP according to the manufacturer's protocol. Afterward, DAPI was added to mark the nuclei. To examine adipogenesis, cells were rinsed by Milli-Q water after fixation with 4% paraformaldehyde, and then treated with fresh Oil Red O (Sigma) solution in 60% isopropanol for 30 min and rinsed by 60% isopropanol and Milli-Q water. Cell nuclei were also labeled by DAPI. The cells containing lipids were identified as adipocytes. The stained cells were observed in the inverted microscope mounted with a color camera (Zeiss Axio Observer Z1, Germany). Micrographs were captured for post statistical analysis. The fraction of osteogenesis and adipogenesis of cells in different roughness regions were calculated by counting the number of cells in more than three randomly selected fields (10 × magnification) and normalizing to the total number of cells detected by DAPI staining in each individual sample.

**Statistical Analysis:** Data were represented as mean ± standard deviation (SD). Group differences were conducted by one-way analysis of variance with Tukey's post hoc test. *p*-Values < 0.05 were considered as statistically significant (\**p* < 0.05, \*\**p* < 0.01, \*\*\**p* < 0.001, \*\*\*\**p* < 0.0001). All statistical analyses were performed with GraphPad Prism 8.

## Supporting Information

Supporting Information is available from the Wiley Online Library or from the author.

## Acknowledgements

The authors acknowledge the financial support from National Natural Science Foundation of China (Grant No. 51973129), State Key Laboratory of Polymer Materials Engineering, Sichuan University (grant no. sklpm2018-3-09), and China Scholarship Council. The authors thank the Core Facility BioSupraMol (Free University of Berlin, Germany) for the assistance in SEM and confocal microscopy measurements support. The authors thank Dr. Pamela Winchester for her careful language polishing of the manuscript.

Note: An error in the  $R_a$  for RG<sub>50%</sub>, located in line 9 of the 2nd paragraph of Section 2.1, was corrected on 12 March 2020 after original online publication.

## Conflict of Interest

The authors declare no conflict of interest.

## Keywords

cell adhesion, cell differentiation, mechanotransduction, mesenchymal stem cells, roughness gradient

Received: September 23, 2019

Revised: November 28, 2019

Published online: February 17, 2020

- [1] J. D. Humphrey, E. R. Dufresne, M. A. Schwartz, *Nat. Rev. Mol. Cell Biol.* **2014**, *15*, 802.
- [2] D. Kim, P. P. Provenzano, C. L. Smith, A. Levchenko, *J. Cell Biol.* **2012**, *197*, 351.
- [3] J. Eyckmans, T. Boudou, X. Yu, C. S. Chen, *Dev. Cell* **2011**, *21*, 35.
- [4] J. Park, D. Kim, A. Levchenko, C. Allan, A. Ker, C. L. C. Smith, P. M. Tsimbouri, J. Borsoi, S. O. Neill, N. Gadegaard, *Nano Lett.* **2018**, *18*, 1.
- [5] H. Wolfenson, B. Yang, M. P. Sheetz, *Annu. Rev. Physiol.* **2019**, *81*, 585.
- [6] M. Bao, J. Xie, W. T. S. Huck, *Adv. Sci.* **2018**, *5*, 1800448.
- [7] T. Sjöström, M. J. Dalby, A. Hart, R. Tare, R. O. C. Oreffo, B. Su, *Acta Biomater.* **2009**, *5*, 1433.
- [8] D. Khang, J. Choi, Y. M. Im, Y. J. Kim, J. H. Jang, S. S. Kang, T. H. Nam, J. Song, J. W. Park, *Biomaterials* **2012**, *33*, 5997.
- [9] K. Cai, J. Bossert, K. D. Jandt, *Colloids Surf., B* **2006**, *49*, 136.
- [10] A. B. Faia-Torres, S. Guimond-Lischer, M. Rottmar, M. Charnley, T. Goren, K. Maniura-Weber, N. D. Spencer, R. L. Reis, M. Textor, N. M. Neves, *Biomaterials* **2014**, *35*, 9023.
- [11] Q. Flamant, A. M. Stanciuc, H. Pavailler, C. M. Sprecher, M. Alini, M. Peroglio, M. Anglada, *J. Biomed. Mater. Res., Part A* **2016**, *104*, 2502.
- [12] Q. Wei, K. Achazi, H. Liebe, A. Schulz, P. L. M. Noeske, I. Grunwald, R. Haag, *Angew. Chem., Int. Ed.* **2014**, *53*, 11650.
- [13] C. Schlaich, L. Cuellar Camacho, L. Yu, K. Achazi, Q. Wei, R. Haag, *ACS Appl. Mater. Interfaces* **2016**, *8*, 29117.
- [14] F. Ye, B. G. Petrich, P. Anekal, C. T. Lefort, A. Kasirer-Friede, S. J. Shattil, R. Ruppert, M. Moser, R. Fässler, M. H. Ginsberg, *Curr. Biol.* **2013**, *23*, 2288.
- [15] S. H. Ku, J. Ryu, S. K. Hong, H. Lee, C. B. Park, *Biomaterials* **2010**, *31*, 2535.
- [16] J. Albuschies, V. Vogel, *Sci. Rep.* **2013**, *3*, 1658.
- [17] M. J. Dalby, N. Gadegaard, M. O. Riehle, C. D. W. Wilkinson, A. S. G. Curtis, *Int. J. Biochem. Cell Biol.* **2004**, *36*, 2005.

- [18] H. Chang, Y. Wang, *InTechOpen* (Ed: D. Eberli), Rijeka, Croatia **2011**, pp. 569–588.
- [19] K. Anselme, L. Ploux, A. Ponche, *J. Adhes. Sci. Technol.* **2010**, *24*, 831.
- [20] A. W. Feinberg, W. R. Wilkerson, C. A. Seeger, A. L. Gibson, L. Hoipkemeier-Wilson, A. B. Brennan, *J. Biomed. Mater. Res., Part A* **2008**, *86A*, 522.
- [21] D. Lepzelter, O. Bates, M. Zaman, *Langmuir* **2012**, *28*, 5379.
- [22] Q. Wei, T. Becherer, S. Angioletti-Uberti, J. Dzubiella, C. Wischke, A. T. Neffe, A. Lendlein, M. Ballauff, R. Haag, *Angew. Chem., Int. Ed.* **2014**, *53*, 8004.
- [23] D. Choquet, D. P. Felsenfeld, M. P. Sheetz, *Cell* **1997**, *88*, 39.
- [24] M. Aragona, T. Panciera, A. Manfrin, S. Giullitti, F. Michielin, N. Elvassore, S. Dupont, S. Piccolo, *Cell* **2013**, *154*, 1047.
- [25] S. H. D. Wong, B. Yin, B. Yang, S. Lin, R. Li, Q. Feng, H. Yang, L. Zhang, Z. Yang, G. Li, C. H. J. Choi, L. Bian, *Adv. Funct. Mater.* **2019**, *29*, 1806822.
- [26] B. K. K. Teo, S. T. Wong, C. K. Lim, T. Y. S. Kung, C. H. Yap, Y. Ramagopal, L. H. Romer, E. K. F. Yim, *ACS Nano* **2013**, *7*, 4785.
- [27] B. Geiger, J. P. Spatz, A. D. Bershadsky, *Nat. Rev. Mol. Cell Biol.* **2009**, *10*, 21.
- [28] B. K. Chauhan, A. Disanza, S.-Y. Choi, S. C. Faber, M. Lou, H. E. Beggs, G. Scita, Y. Zheng, R. A. Lang, *Development* **2009**, *136*, 3657.
- [29] J. P. Myers, E. Robles, A. Ducharme-Smith, T. M. Gomez, *J. Cell Sci.* **2012**, *125*, 2918.
- [30] E. Makhija, D. S. Jokhun, G. V. Shivashankar, *Proc. Natl. Acad. Sci. U. S. A.* **2016**, *113*, E32.
- [31] J. H. Lee, D. H. Kim, H. H. Lee, H. W. Kim, *Biomaterials* **2019**, *197*, 60.
- [32] J. Swift, I. L. Ivanovska, A. Buxboim, T. Harada, P. C. D. P. Dingal, J. Pinter, J. D. Pajeroski, K. R. Spinler, J. W. Shin, M. Tewari, F. Rehfeldt, D. W. Speicher, D. E. Discher, *Science* **2013**, *341*, 1240104.
- [33] S. J. Heo, T. P. Driscoll, S. D. Thorpe, N. L. Nerurkar, B. M. Baker, M. T. Yang, C. S. Chen, D. A. Lee, R. L. Mauck, *eLife* **2016**, *5*, e18207.
- [34] K. Anselme, N. T. Wakhloo, P. Rougerie, L. Pieuchot, *Adv. Healthcare Mater.* **2018**, *7*, 1701154.
- [35] J. Lammerding, L. G. Fong, J. Y. Ji, K. Reue, C. L. Stewart, S. G. Young, R. T. Lee, *J. Biol. Chem.* **2006**, *281*, 25768.
- [36] A. Buxboim, J. Irianto, J. Swift, A. Athirasala, J.-W. Shin, F. Rehfeldt, D. E. Discher, *Mol. Biol. Cell* **2017**, *28*, 3333.
- [37] J. K. Kim, A. Louhghalam, G. Lee, B. W. Schafer, D. Wirtz, D. H. Kim, *Nat. Commun.* **2017**, *8*, 1.
- [38] A. R. Killars, J. C. Grim, C. J. Walker, E. A. Hushka, T. E. Brown, K. S. Anseth, *Adv. Sci.* **2019**, *6*, 1801483.
- [39] S. Dupont, L. Morsut, M. Aragona, E. Enzo, S. Giullitti, M. Cordenonsi, F. Zanconato, J. Le Digabel, M. Forcato, S. Bicciato, N. Elvassore, S. Piccolo, *Nature* **2011**, *474*, 179.
- [40] S. R. Caliri, S. L. Vega, M. Kwon, E. M. Soulas, J. A. Burdick, *Biomaterials* **2016**, *103*, 314.
- [41] G. Abagnale, M. Steger, V. H. Nguyen, N. Hersch, A. Sechi, S. Jousen, B. Denecke, R. Merkel, B. Hoffmann, A. Dreser, U. Schnakenberg, A. Gillner, W. Wagner, *Biomaterials* **2015**, *61*, 316.
- [42] A. R. Cameron, J. E. Frith, J. J. Cooper-White, *Biomaterials* **2011**, *32*, 5979.
- [43] J. N. Roberts, J. K. Sahoo, L. E. McNamara, K. V. Burgess, J. Yang, E. V. Alakpa, H. J. Anderson, J. Hay, L. A. Turner, S. J. Yarwood, M. Zelzer, R. O. C. Oreffo, R. V. Ulijn, M. J. Dalby, *ACS Nano* **2016**, *10*, 6667.
- [44] M. Jaggy, P. Zhang, A. M. Greiner, T. J. Autenrieth, V. Nedashkivska, A. N. Efremov, C. Blattner, M. Bastmeyer, P. A. Levkin, *Nano Lett.* **2015**, *15*, 7146.
- [45] D. Hevia, A. Rodriguez-Garcia, M. Alonso-Gervós, I. Quirós-González, H. M. Cima-devilla, C. Gómez-Cordovés, R. M. Sainz, J. C. Mayo, D. Hevia, A. Rodriguez-Garcia, *Protoc. Exch.* **2011**, <https://doi.org/10.1038/protex.2011.272>.